

Throw partitioning across normal fault zones in the Ptolemais Basin, Greece

EFSTRATIOS DELOGKOS^{1*}, TOM MANZOCCHI¹, CONRAD CHILDS¹,
CHRISTOS SACHANIDIS², TRYFON BARBAS², MARTIN P. J. SCHÖPFER³,
ALEXANDROS CHATZIPETROS⁴, SPYROS PAVLIDES⁴ & JOHN J. WALSH¹

¹*Fault Analysis Group, School of Earth Sciences, University College Dublin, Belfield, Dublin 4, Ireland*

²*Public Power Corporation of Greece, Western Macedonian Lignite Centre, Ptolemais, Greece*

³*Department for Geodynamics and Sedimentology, University of Vienna, Althanstrasse 14, A-1090 Vienna, Austria*

⁴*Department of Geology, Aristotle University of Thessaloniki, Thessaloniki, Greece*

*Correspondence: stratos.delogkos@ucd.ie

Abstract: The total throw across a fault zone may not occur entirely on a single fault strand but may be distributed onto several strands or may be accommodated by distributed deformation within or adjacent to the fault zone. Here we conduct a quantitative analysis of the partitioning of throw into three components, the throw accommodated by: (a) the largest fault strand; (b) subsidiary faults; and (c) continuous deformation in the form of bed rotation in sympathy with the fault downthrow direction. This analysis is applied to seven seismic-scale fault zones at outcrop resolution (maximum throw 50 m) that were mapped over a four-year period during open-cast lignite mining within the late Miocene–Pliocene Ptolemais Basin, West Macedonia, Greece. The analysis shows that the fault zones offsetting the lignite–marl sequence are more localized at higher throws with progressively more of the total throw accommodated by the largest fault strand. Normal drag, which can account for up to 12 m of the total throw, accommodates a lower proportion of the total throw on larger faults. It appears that initial fault segmentation is the main control on the degree of, and spatial variation in, fault throw partitioning.



Gold Open Access: This article is published under the terms of the CC-BY 3.0 license

Fault zones are complex features that can comprise multiple slip surfaces and heterogeneously distributed fault rock of various compositions. This complex structure, and its variability over different scales of inspection, make consistent descriptions of fault zone structure difficult (Ben-Zion & Sammis 2003). In recent years, fault zones have been most often described in terms of a central high strain ‘core’ that accommodates most of the fault throw and an enveloping damage zone that contains minor structures that accommodate wall-rock strains and some, relatively minor, proportion of the total fault throw. Quantification of fault zone structure has generally concentrated on determining the widths of different fault zone components, such as fault core, damage zone and fault rock, and on using these measurements as indicators for fault zone structural evolution (Evans 1990; Caine *et al.* 1996; Shipton & Cowie 2001; Childs *et al.* 2009). In this paper, we are concerned with how throw is partitioned onto the different components of a fault zone (Fig.

1). This approach is based on conceptual models of how fault zones develop that suggest throw partitioning within fault zones should provide a record of how faults grow. For example, it is widely accepted that one of the main mechanisms by which faults increase their length is by linkage between segments, and this linkage should be recorded in the amount of throw accommodated by fault splays that were by-passed when fault segments coalesced to form a continuous fault surface (Peacock & Sanderson 1991; Childs *et al.* 1995, 2009; Cartwright *et al.* 1996; Walsh *et al.* 1999). Similarly, measurement of the proportion of throw accommodated by ductile deformation on faults of different sizes can test models in which faulting is preceded by the formation of a precursory monocline or a process zone (Billings 1972; Reches & Eidelman 1995; Peacock *et al.* 2000; Brandes & Tanner 2014). Partitioning of throw onto the various components of a fault zone can be an important factor providing insights into the growth of fault zones and in determining

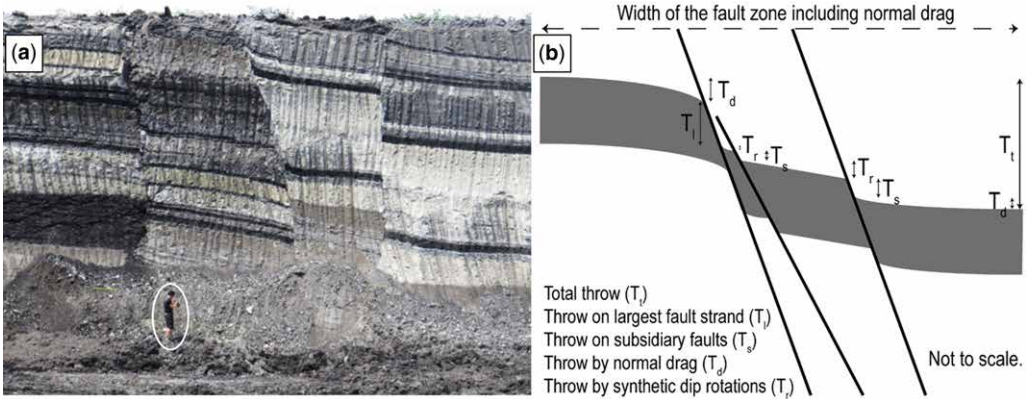


Fig. 1. (a) Outcrop photograph of a fault zone in the Kardia mine showing that the total throw (c. 13 m) is accommodated by several fault strands and by continuous deformation within and adjacent to the fault zone (person circled for scale). (b) Schematic diagram showing the partitioning of total throw (T_t) into discontinuous throw, comprising the largest fault strand (T_l) and subsidiary synthetic faults (T_s), and continuous throw, comprising synthetic dip rotation (T_r) and normal drag (T_d) components.

across-fault reservoir juxtaposition, and thus the flow properties of faults in the subsurface (Caine *et al.* 1996; Childs *et al.* 1997; Wibberley *et al.* 2008; Manzocchi *et al.* 2010; Seebeck *et al.* 2014). Despite this importance, quantification of the frequency and magnitude of throw partitioning has not received much attention in the published literature.

In general, recorded fault throws can be divided into two components: discontinuous and continuous throws. Discontinuous throw refers to throw that occurs on discrete fault surfaces, and continuous throw refers to throw accommodated by deformation of the wall rock due to normal drag and bed rotations within the fault zone (Fig. 1b). The term ‘normal drag’ is used here in a purely geometrical sense (e.g. Peacock *et al.* 2000) and does not imply a formation mechanism. In this paper, we subdivide the discontinuous throw into the throw on the largest fault strand and the remaining component, which is the sum of throws on subsidiary synthetic fault strands (Fig. 1b).

Throw partitioning has been previously used as an indicator of fault zone development. Jamison & Stearns (1982) described a transition from distributed deformation bands to discrete fault slip surfaces at a throw of approximately 10 m in normal faults formed in high-porosity sandstones. Kristensen (2005) found that the throw on the largest fault strand within a fault zone is frequently less than half, and often as low as 30%, of the total throw on centimetre-scale faults in clay/sand sequences. A compilation by Freeman *et al.* (2008) shows that the proportion of throw accommodated on the largest segment in a fault zone is, in general, hugely variable. In a study of the Hidden Valley normal

fault at Canyon Lake Gorge, Ferrill *et al.* (2011) concluded that the width of the fault damage zone associated with this 60 m displacement fault was established early during the growth of the fault, with later progressive localization of displacement. They also estimated that the actual stratigraphic displacement is overestimated by about 14–21% due to displacement partitioning across a fault zone. Manzocchi *et al.* (2008) proposed a quantitative function based on a similar conceptual model of damage zone evolution and displacement localization, and in a modelling study demonstrated that the effect of realistic fault displacement partitioning on full-field oil production can, in some circumstances, be significant.

In this paper, we augment these available quantitative datasets addressing displacement partitioning in normal faults. Specifically, we measure how the throw at various positions within seven fault zones is partitioned onto the largest fault surface, subsidiary synthetic fault surfaces and ductile components, with the aim of better understanding how each of these three components contributes to the total throw as fault throw increases.

Data and methodology

The dataset used in this study is derived from the Kardia Mine (also known as the Tomeas Eksi Mine), which is one of the four active, open-pit lignite fields in the Ptolemais Basin, west Macedonia, Greece (Fig. 2). The Ptolemais Basin is an elongate intramontane lacustrine basin and is part of the Florina–Ptolemais–Servia Basin, which is a NNW–SSE-trending graben system that extends

THROW PARTITIONING ACROSS NORMAL FAULT ZONES

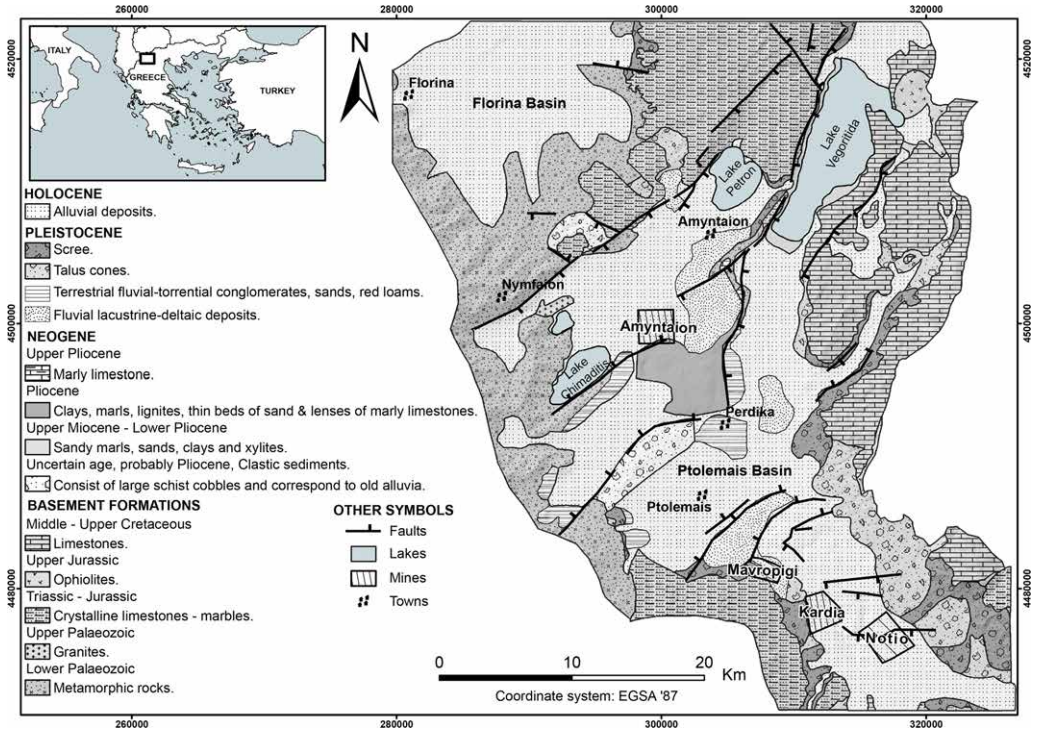


Fig. 2. Geological map of the Ptolemais Basin showing the major fault structures and the locations of the four active, open-pit lignite mines (modified after Pavlides 1985).

over a distance of 120 km from Bitola in the Former Yugoslav Republic of Macedonia to the village of Servia, SE of Ptolemais, Greece (Pavlides 1985). The basin is affected by two fault systems related to two extensional episodes (Pavlides & Mountrakis 1987; Mercier *et al.* 1989). The first, Late Miocene episode resulted in the formation of the basin in response to NE–SW extension. The second episode was a NW–SE extension during the Quaternary, resulting in the NE–SW-striking normal faults that currently bound a number of sub-basins, including the basins of Florina, Ptolemais and Servia (Pavlides & Mountrakis 1987).

There is little surface evidence of the Late Miocene NW–SE-striking faults that control the basin margins, although their presence is confirmed from boreholes (Pavlides & Mountrakis 1987) and from some recent exposures along the western margin of the Ptolemais Basin. The surface geology is dominated by the Quaternary faults, which have orientations ranging from the expected NE–SW strikes to the north of the region, to NNE–SSW orientations to the north of the Mavropigi Mine, and through to approximately east–west strikes in the vicinity of the Kardja and Notio mines (Fig. 2). Some of the Quaternary-age NE–SW-striking normal faults

have been activated recently, causing both weak and strong earthquakes (Pavlides *et al.* 1995; Mountrakis *et al.* 1998).

The basin is filled with a 500–600 m-thick succession of Late Miocene–Pleistocene lake sediments with intercalated lignites and alluvial deposits, which are divided into three basin-wide lithostratigraphic units: the Lower Formation; the Ptolemais Formation; and the Upper Formation (Anastopoulos & Koukouzas 1972; Steenbrink *et al.* 1999). This work has concentrated on faults in the Ptolemais Formation, which has a thickness of approximately 110 m, and consists of a rhythmic alternation of metre-scale lignite and lacustrine marl beds with intercalated fluvial sands and silts, and some 20 volcanic ash beds. This formation was dated as early Pliocene using a combination of magneto- and cyclostratigraphy, and $^{40}\text{Ar}/^{39}\text{Ar}$ dating (van Vugt *et al.* 1998; Steenbrink *et al.* 1999).

In addition to the normal faults, the mines contain fault-related folding (Fig. 3) in the form of reverse and normal drag (discussed in more detail in a later section). Furthermore, one of the mines, Notio Mine, contains thrusts that predate Quaternary faults but have identical strikes. It has been suggested (Diamantopoulos *et al.* 2013) that the

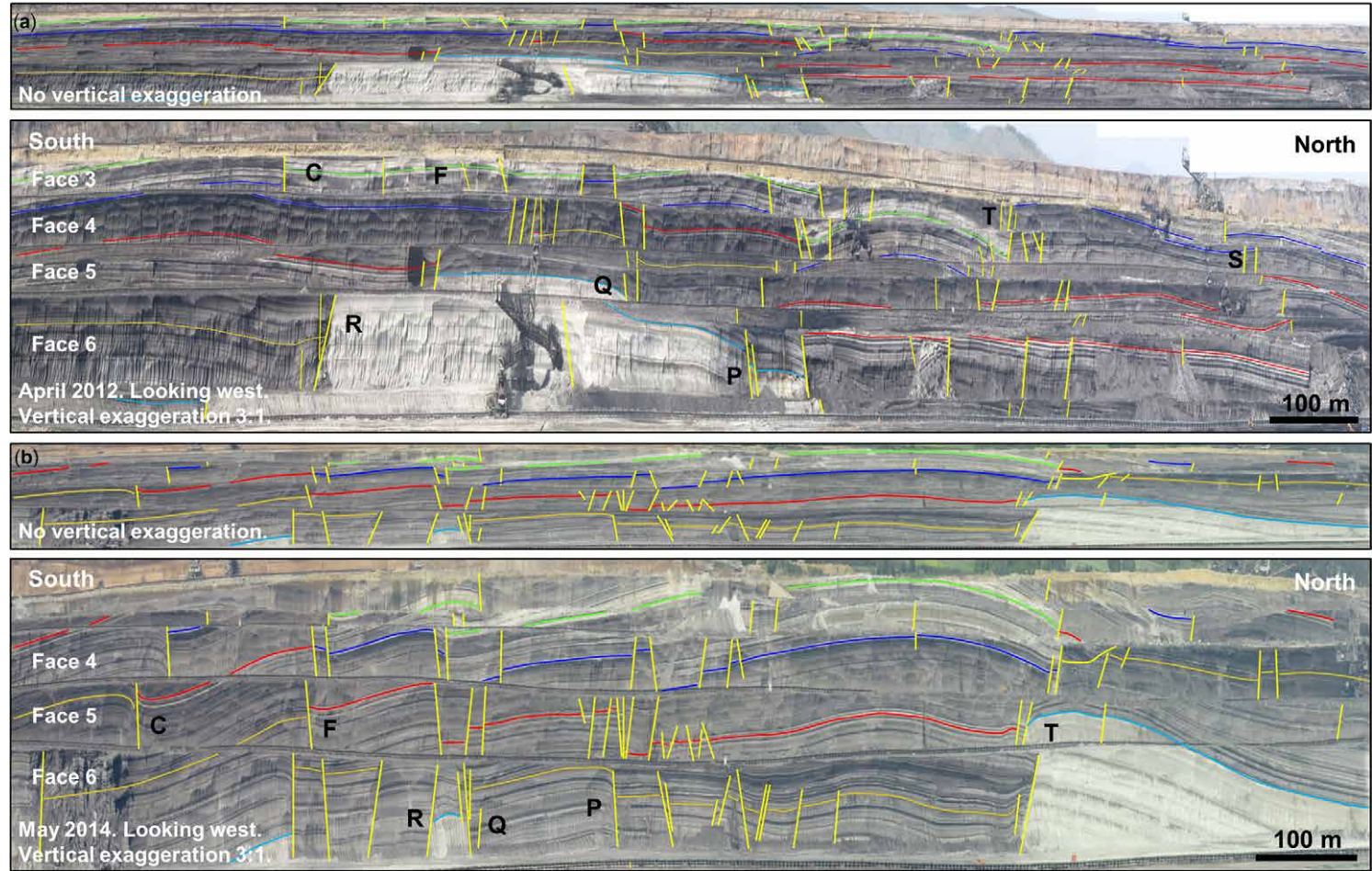


Fig. 3. True scale and $\times 3$ vertically exaggerated panoramic view of the active, open-cast, Kardia Mine in (a) April 2012 and (b) May 2014. Faults are drawn as yellow lines and a selection of horizons is highlighted. The letters (C, F, R, Q, P, T and S) are the names of the interpreted fault zones.

THROW PARTITIONING ACROSS NORMAL FAULT ZONES

normal faults and thrusts are associated with extension above, and compression below, a neutral surface associated with folds developed in an active transpressional zone. However, our mapping shows that the thrusts at the Notio Mine are contained within a well-defined approximately 30 m-thick unit bounded by a décollement at the base and an unconformity at the top. We interpret this unit to represent a synsedimentary subaqueous landslide, with the presence of geometries similar to, but on a larger scale than, those contained in soft sediments in the Dead Sea described by Alsop & Marco (2013). Therefore, the thrusts are not associated with tectonic compression, but instead are of very early, synsedimentary gravity-driven origin. The thrusts are consistently cross-cut by the normal faults and occasionally reactivated as normal faults, providing further evidence for the early timing of the thrusts. Our interpretation of synsedimentary slumping followed by normal faulting and fault-related folding is significantly different to the model for these structures suggested by Diamantopoulos *et al.* (2013), which requires a transtensional-dominated regime.

Kardia Mine: 3D structural model

The Kardia Lignite Mine is located in the central part of the Neogene lignite basin and is dominated by east–west-trending Quaternary normal faults. It consists of seven principal mining faces, which are, on average, 2.5 km long. The *c.* 20 m-high mining faces step to the west from the bottom to the top of the mine, and are separated by benches that have widths of *c.* 50–100 m. We have visited and mapped the mine 16 times at approximately three-month intervals from October 2009 to May 2014. During each interval, each face was taken back by between 20 and 50 m. The data collected during each fieldwork campaign were photographs at various resolutions, and accurate GPS locations, structural measurements and interpretations of all exposed faults and related structures observed in the mine, such as normal or reverse drag.

Three-dimensional models of the faults in the Kardia Mine were produced by placing our fully georeferenced data within a 3D structural interpretation package (Fig. 4a). Each of the mining faces was cropped from the panoramic photographs and imported into the 3D database. The outcome was a data volume similar in format and scale to a 2D seismic reflection survey, but with outcrop-scale resolution. Horizons and faults were interpreted in a similar fashion to a 2D seismic survey, but with the aid of detailed field observations.

Each fault zone was mapped from about 100 fault-perpendicular cross-sections, which together typically cover areas of the fault surface *c.* 1100 m

long and up to 80 m high (Figs 4 & 5). The striking colour contrast between the lignite and marl layers makes these sediments ideal for detailed throw analysis in cross-section and along-strike, as individual horizons are continuous on the scale of the structures investigated. In total, 14 horizons were mapped within a 110 m stratigraphic interval, and these were used to calculate discontinuous throws for each of the interpreted fault surfaces (Figs 4 & 5). Figure 5 shows one of the interpreted horizons in map view with the footwall and hanging-wall fault cutoffs. Note that, owing to the excavation direction, deeper horizons in the sequence cover most of the eastern part of the mine and shallower horizons cover most of the western part.

Main characteristics of faults in the Ptolemais Basin

In an area of 2.5 km², we mapped seven fault zones (labelled C, F, R, Q, P, T and S in Figs 3–5) that displace the lignite–marl sequence by up to 50 m. These seven fault zones consist of more than 115 mapped fault segments. Fault segments less than approximately 35 m long are not mappable in 3D as they are shorter than the lateral, along-strike, resolution of this dataset. Only fault zone S, with a maximum throw of 18.5 m, has been mapped over its entire length (maximum recorded length of 630 m). For five fault zones (C, F, P, R and T), one of the two tips has been mapped; and for fault zone Q, neither of the two tips lie in the area that this dataset covers. Several individual fault segments were mapped from tip to tip, with the largest – a segment in fault zone P – having a maximum length of 550 m and maximum discontinuous throw of 33 m.

Grouping of the fault segments into a fault zone can be highly subjective and depends largely on the scale of faulting relative to the mapped area. Fault segments are considered here to be part of the same fault zone if they interact with each other by soft and/or hard linkage (Walsh & Watterson 1991; Walsh *et al.* 2003), as indicated by the occurrence of a simple aggregate throw profile that includes the throw accommodated by continuous deformation. Some of the interpreted fault zones are larger than the sample area and it may be that, given a larger sample area, interactions between separate fault zones may become apparent, so that the fault zones would be grouped differently.

Fault rock

The faults in the Ptolemais mines have anomalously high fault displacement to fault rock thickness ratios compared to normal faults in other areas. Wide

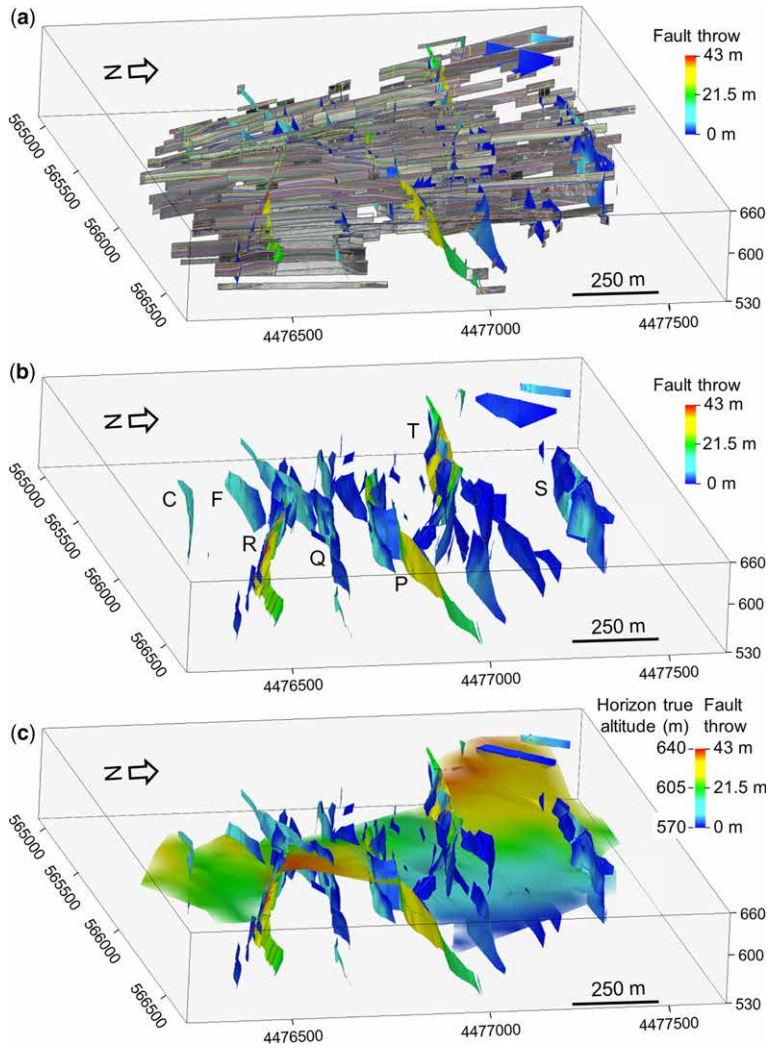


Fig. 4. Oblique view of a 3D model of Kardia Mine showing (a) all the mining faces imported into a 3D structural interpretation package, including the interpretation of seven fault zones that displace the lignite–marl sequence by up to 50 m. The colours on the fault surfaces are contours of throw. (b) As (a), but excluding the imported mining faces. The letters are the names assigned to each fault zone. (c) As (b), but including one of the interpreted horizons, which is displaced by the faults and is located near the middle of the exposed stratigraphic sequence. The horizon is coloured for height above sea level.

zones of fault rock (e.g. breccias) are not developed in these faults. Small-scale lenses and splays that, with increasing displacement, would be pulverized and converted into fault rock in other lithologies, are fortuitously preserved in these rocks, allowing throw partitioning to be examined at high strains.

Throw gradients

Throw gradients on individual fault segments, and also on whole fault zones, are larger here (average

value of *c.* 0.125) than in many other fault systems (cf. Walsh *et al.* 2002; Bailey *et al.* 2005; Kim & Sanderson 2005; Ferrill *et al.* 2008; Schultz *et al.* 2008). This observation is compatible with the overall impression that these faults are more highly segmented than usual. Mechanical differences between lignite and marl do not exert a strong control on throw gradients. Instead, fault geometry exerts the primary control and so that the highest throw gradients are associated with interacting fault tips.

THROW PARTITIONING ACROSS NORMAL FAULT ZONES

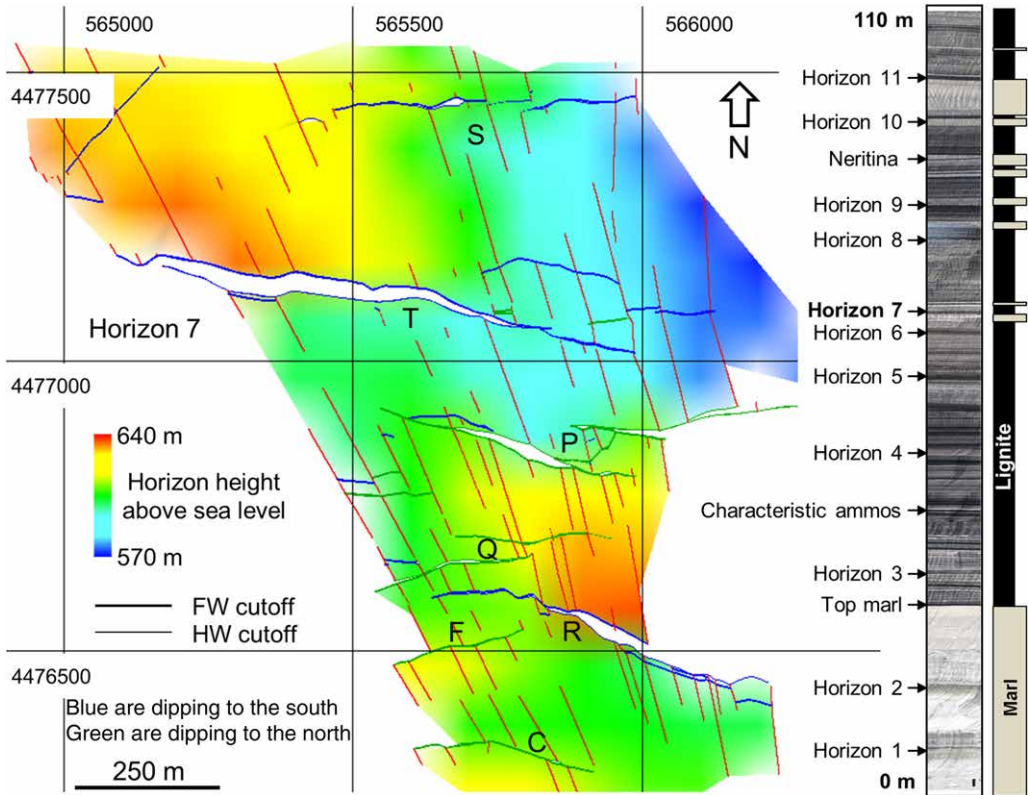


Fig. 5. Map view of one of 14 interpreted horizons, including the footwall (FW) and hanging-wall (HW) cutoffs of each interpreted fault. Faults with blue polygons are dipping to the south and those with green polygons to the north. The letters (C, F, R, Q, P, T and S) are the names of the interpreted fault zones. The colours show the height above sea level. The red lines show the locations of the outcrop photographs used to map this horizon. On the right is the exposed stratigraphic sequence accompanied by a simplified lithological column, indicating the locations of the interpreted horizons. The layers of Neritina (*Theodoxus macedonicus*) and Characteristic Ammos (volcanic ash) are basin-wide.

Fault-related folding

Vertically exaggerated field photographs (Fig. 3) clearly show folds present in the mine. The folds are spatially related to the faults displaying normal and reverse drag geometries, which indicates that they are part of the same geological deformation event. Like Ferrill *et al.* (2012), we do not consider a frictional drag mechanism to be important in the development of normal drag structures in the mine. Reverse drag refers to folding adjacent to a fault plane, so that the layers are concave towards the slip direction (Barnett *et al.* 1987). Reverse drag is a much larger scale feature than normal drag and defines the displacement field associated with the faults. Often it is difficult to identify reverse drag in the field, especially in areas of high fault density. We expect greater expression of reverse drag on the hanging wall rather than on the footwall

of the normal faults in the Ptolemais Basin, as Doutsos & Koukouvelas (1998) estimated a footwall uplift/hanging-wall subsidence ratio of 1:2 for these faults. The vertically exaggerated panoramic view of the Kardia Mine (Fig. 3) shows clearly reverse drag structures on the hanging wall of fault zones R and T. Figure 3a also shows the product of opposing reverse drag zones, in the form of an anticline, between the two opposite-dipping large fault zones, P and T. Normal and reverse drag can often occur on the same fault (e.g. Fig. 3b, fault zone T at face 6), with the reverse drag occurring over a much larger distance, but with relatively lower bed rotations (cf. Hamblin 1965).

Another form of folding related to the faults in Ptolemais are monoclines in which a geometrical offset is observed over a localized volume of rock, but where no discrete faults are formed. A partly faulted monocline structure exists in fault zone

Q (Figs 4 & 6f), overlying an array of soft-linked fault segments. Monoclines can also be observed at the tips of individual fault segments. A well-developed monocline (Fig. 7e) occupies the volume around the tip of the footwall segment of a relay zone in fault zone P (Fig. 7).

The origin of monoclines and normal drag may be related. For instance, monoclines might be the predominant feature of a fault zone at a very early growth stage and, as the fault zone grows, they might become faulted and preserved as footwall and/or hanging-wall normal drag (Sharp *et al.* 2000; White & Crider 2006).

Synsedimentary faulting

Sediment thickness changes across faults indicate that some fault zones were active during deposition of the Ptolemais Formation (fault zones P and T), but the majority of faults grew mainly after the deposition of the Ptolemais Formation. Therefore, there is no evidence of widespread synsedimentary fault movement in these mines, an observation which is compatible with the chronology of extension and sedimentation for the basin established by Pavlides & Mountrakis (1987). Based on the regional thickness of the Quaternary sediments and the timing of faulting, these faults were formed in a depth ranging from 0 to approximately 500 m.

Fault zone characteristics

In this section we provide some details of the geometry and structure of individual fault zones studied in this paper to give an impression of some of the typical features of these zones, and of variability of structure within and between the fault zones. Selected features of these fault zones are referred to in later sections. Below, we subdivide the fault zones into lower (maximum throw 17–23 m) and higher (maximum throw 44.5–50.5 m) displacement faults.

Lower displacement fault zones

Fault zone S (Figs 3–5) has a maximum throw of 18.5 m and comprises multiple en echelon fault segments with both soft- and hard-linkages between adjacent segments. The average width of the fault zone, including the contribution from normal drag, is 50 m. If drag is not taken into account the zone is, on average, 15 m wide.

As mentioned previously, a typical example of a monoclinial structure occurs in fault zone Q (Figs 5 & 6), where an array of soft-linked fault segments underlies and locally displaces a monocline,

so that the dominant feature of the mapped part of this fault zone is an area of pervasive continuous deformation. This area is over 400 m long in the fault-parallel direction (Fig. 6d, e) and has a maximum width of 200 m. The total throw over this portion of the fault zone varies between 10 and 15 m, only a small proportion of which is accommodated by faulting (Fig. 6d) (see Childs *et al.* 2016). Towards the west and east of this structure, where the total throw increases to 22 m (Fig. 6b–e), most of the throw is accommodated by discrete faults, indicating that the monocline accommodates soft linkage between two underlapping large faults. Complementary variations between faulting and continuous deformation are particularly clear on Horizon 7 (Fig. 6c).

Fault zones C and F (Figs 3–5) were mapped along-strike for only 350 and 200 m, respectively, as they were exposed by mine workings only relatively recently. The maximum recorded throw is 23 m for zone C and 17 m for zone F, and both zones are comparatively simple structures, without significant splays or synthetic faults. Most of their total throw is accommodated by a single fault strand and the remainder by a small, but constant, absolute amount of continuous deformation in the form of normal drag (Fig. 8). Their lateral tips are characterized by the occurrence of monoclines, which can accommodate throws of up to 5 m. Based on observations from the other fault zones in the mine, we expect to find these faults to be segmented once more data become available.

Higher displacement fault zones

Fault zone P, with a maximum total throw of 44.5 m, consists of several fault segments. Towards the centre of the mapped zone is a 75 m-wide relay ramp that transfers displacement between two large segments that overlap by 200 m. The segments are linked by a minor breaching fault, which has a throw of 4 m (Fig. 7). Zone P terminates towards the west with the formation of multiple en echelon secondary fault segments (Fig. 7a), similar to those described by McGrath & Davison (1995) and Marchal *et al.* (2003).

In fault zone R (Figs 3–5 & 9), which has a maximum throw of 49 m, most of the throw is accommodated on a dominant fault strand (Fig. 9), which has associated minor synthetic faults in the hanging wall that connect with the main fault down-dip or along-strike. Zone R has an average width (as defined from the discrete faults) of 20 m, which increases from the centre of the fault zone towards the tip line as the zone becomes more segmented.

Fault zone T is the largest mapped fault zone, with a maximum observed total throw of 50 m that increases towards the unexcavated area to the west

THROW PARTITIONING ACROSS NORMAL FAULT ZONES

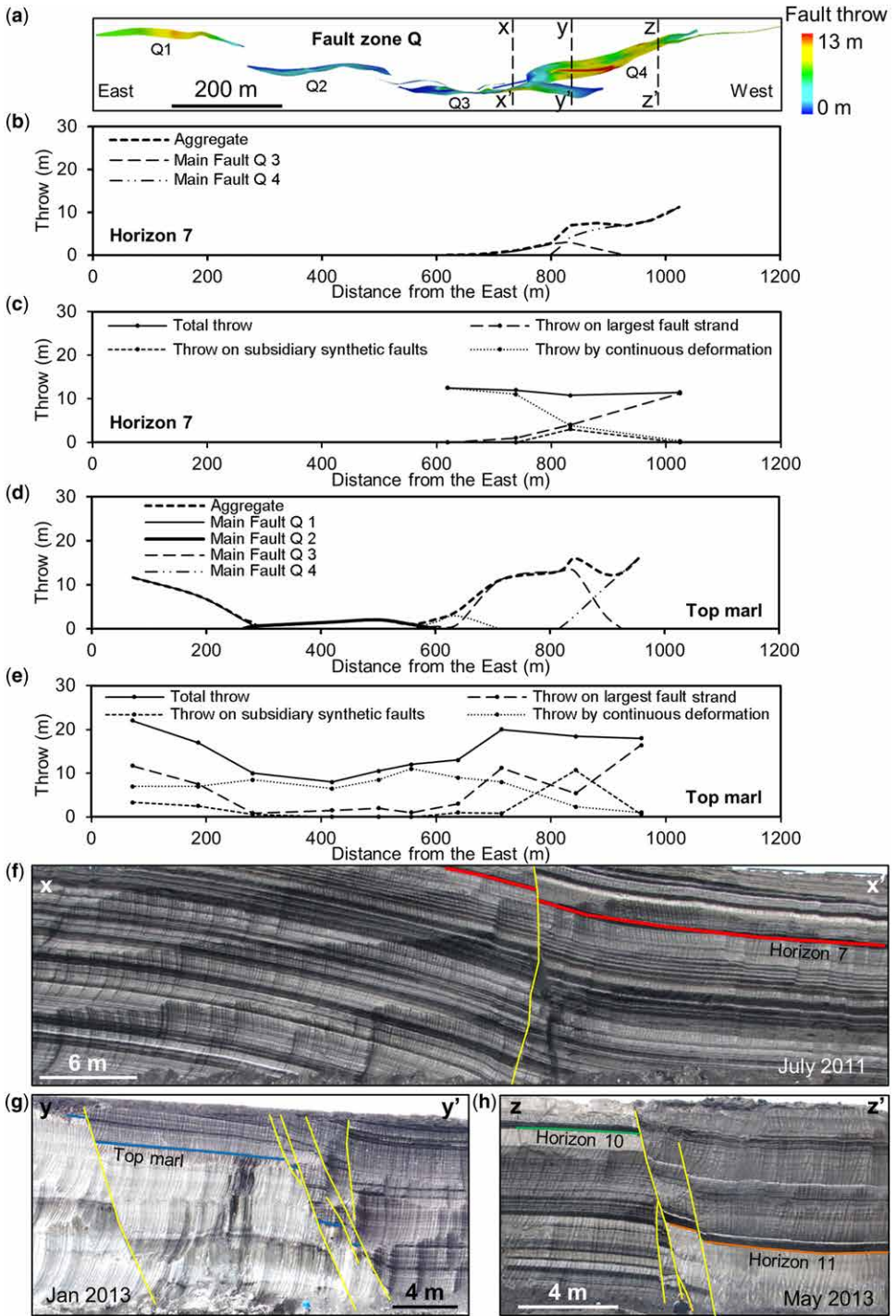


Fig. 6. (a) Plan view of 3D interpreted fault segments comprising zone Q, coloured for throw. (b)–(e) Throw profiles measured on ‘Horizon 7’ and ‘Top Marl’ for the discontinuous throw along each fault segment (b & d) and for each throw component along the fault zone (c & e). The locations of the horizons within the exposed stratigraphic sequence are labelled in Figure 5. (f)–(h) Outcrop photographs of fault zone Q (locations are labelled in a).

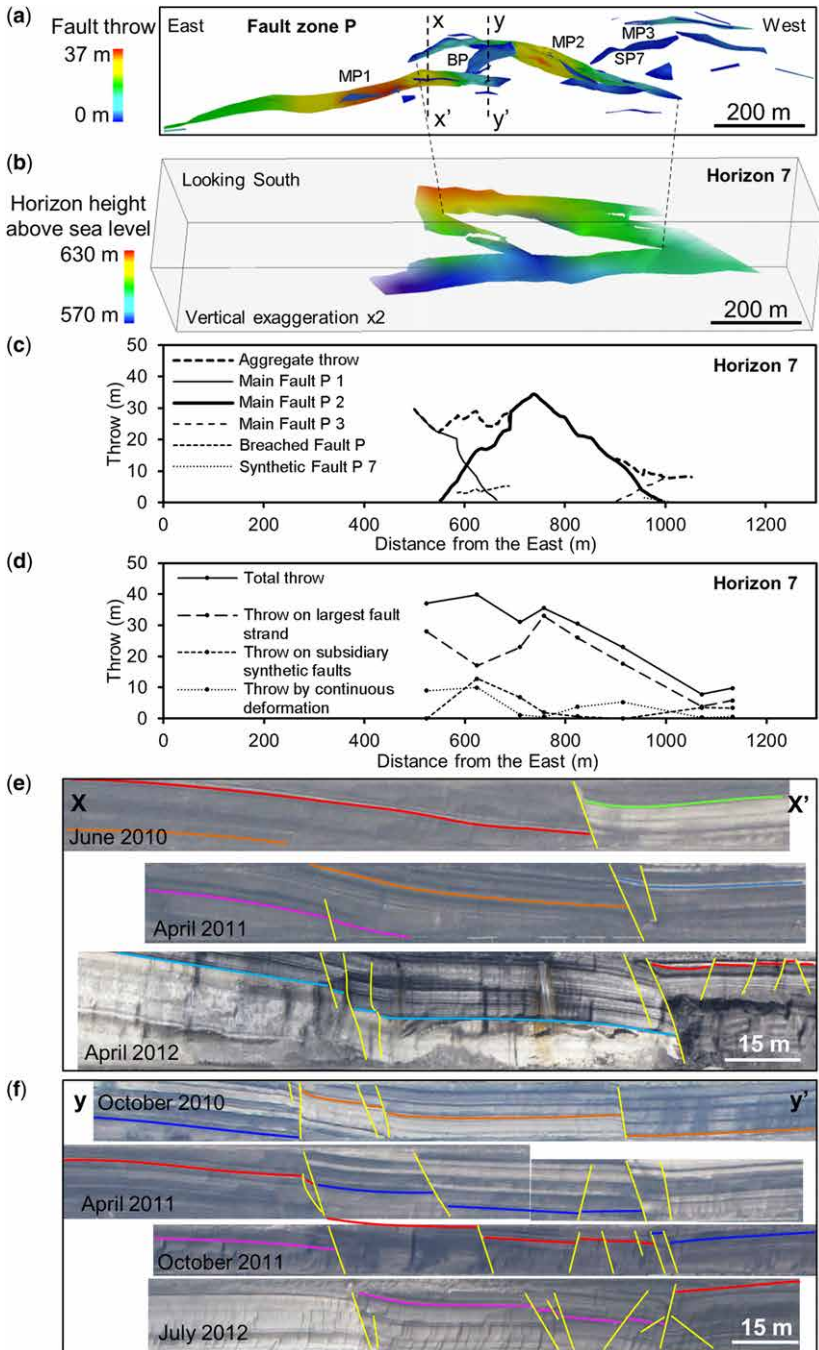


Fig. 7. (a) Plan view of the mapped segments of fault zone P coloured for throw. (b) Lateral view of an interpreted horizon (Horizon 7) coloured for the height above sea level, showing a relay ramp that is transected by a small breaching fault. (c) Throw profiles of the discontinuous throw along each fault segment and (d) of each throw component along the fault zone, measured on Horizon 7. The location of the horizon within the exposed stratigraphic sequence is shown on Figure 5. (e) & (f) Composite cross-sections through fault zone P at the locations shown in (a). Each cross-section is constructed from mine faces at different levels exposed at the dates indicated; the faces that comprise each section are at similar locations and have similar orientations.

THROW PARTITIONING ACROSS NORMAL FAULT ZONES

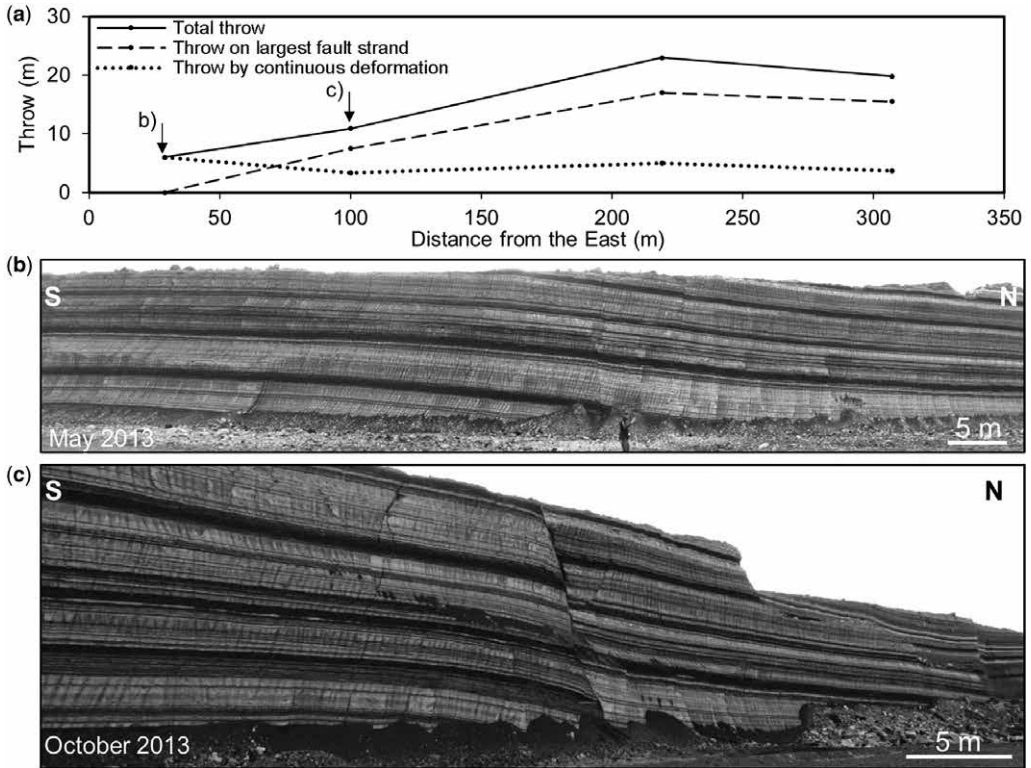


Fig. 8. (a) Profiles of each throw component along the single fault segment that comprises fault zone C. Sections illustrated by outcrop photographs (b) & (c) across the fault segment are labelled in (a).

(Fig. 10). The fault zone tips out to the east within the mapped area. The tip of the fault zone comprises a 600 m-long low-displacement ‘tail’ that consists of multiple small fault segments (Fig. 10d), with an average aggregate throw of 3 m that defines a maximum fault zone width of 300 m. At the western end of this tail (at a distance of *c.* 600 m in Fig. 10b), zone T becomes much narrower and most of the displacement is concentrated onto one main fault strand with minor synthetic faults in the hanging wall (Fig. 10e). This transition is characterized by high-displacement gradients, and the throw increases by 25 m over a distance of 150 m along the main fault trace. To the west of this transition zone, the throw increases more gently to 50 m towards the west boundary of the mine. Recent excavations have revealed a decrease in throw on this fault (‘Main Fault T 1’ in Fig. 10b) that is mirrored by an increase in throw on an adjacent fault 100 m into the footwall (‘Main Fault T 2’ in Fig. 10b), demonstrating larger-scale segmentation of this zone.

The area of increased displacement gradient in fault zone T is attributed to interaction with the opposed-dipping fault zone P. This suggestion is

consistent with the observation that the decrease in throw in fault zone T is mirrored by an increase in throw in fault zone P (Figs 4 & 5) within the area of overlap of these two faults, and is also consistent with the presence of a series of SE–NW-striking minor (throw <1 m) connecting faults in their mutual hanging wall.

Throw partitioning

The total throw on the studied fault zones is separated into three components: the throw on the largest fault strand; the throw on subsidiary synthetic faults; and the throw accommodated by continuous deformation (Fig. 1b). The relative contributions of these components vary spatially over individual fault zones (Figs 6c, e, 7d, 9c & 10c). The distributions of these components also vary between fault zones, and there is no simple pattern that characterizes all seven fault zones. In an effort to identify the general trends and to establish a generalized model for the structure of the fault zones in this area, this section combines data from the seven main fault zones present in the Kardia Mine

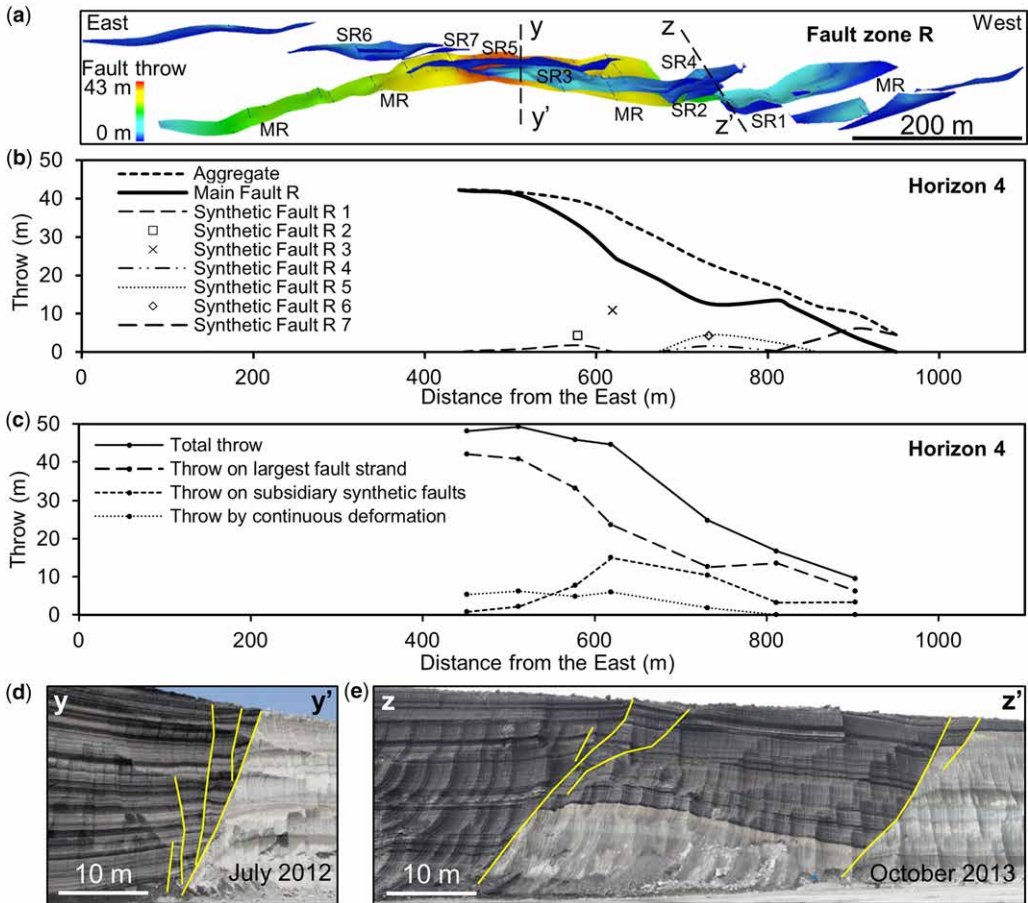


Fig. 9. (a) Plan view of the 3D interpreted fault segments of zone R coloured for throw. (b) Throw profiles of the discontinuous throw along each fault segment and (c) of each throw component along the fault zone measured on Horizon 4. (d) & (e) Outcrop photographs across fault zone R at the locations shown in (a). The locations of the horizons within the exposed stratigraphic sequence are labelled in Figure 5.

(Figs 11 & 12). The data used here are quantitative measures of the three throw components derived from a total of 148 measurements from the seven fault zones. The measurements are taken on cross-sections that are based on several hundred (*c.* 500) mine faces and up to three horizons at different stratigraphic levels over a map sample area of 2.5 km². The total throw is less than 20 m for 70% of the 148 data, and between 20 and 50 m for the remainder (Fig. 11a). For 4% of the data, there are no discrete faults and the total throw is accommodated solely by continuous deformation in the form of monoclines (Fig. 11b). In 20% of the data, there is only one fault strand and in approximately 10% of the data, the fault zone comprises more than four fault strands, with a maximum number of nine strands (Fig. 11b). More

than 80% of the total throw is accommodated by discrete faulting in 50% of the studied cross-sections. In multi-strand fault zones, the sum of the throw that is accommodated by the subsidiary synthetic faults ranges from 1 to 65% of the total throw. The throw accommodated by the main fault strand is less than half of the total throw in 40% of the data.

The relative contributions of the three measured throw components to the total throw are shown in the ternary diagram in Figure 12, and each measured throw component is shown as a function of total throw in Figure 13a, d, g. Examples of cross-sections through fault zones in which the main fault accommodates most of the total throw and the recorded datum lies close to the apex of Figure 12 are provided in Figures 6h, 9d and 10e. Faults

THROW PARTITIONING ACROSS NORMAL FAULT ZONES

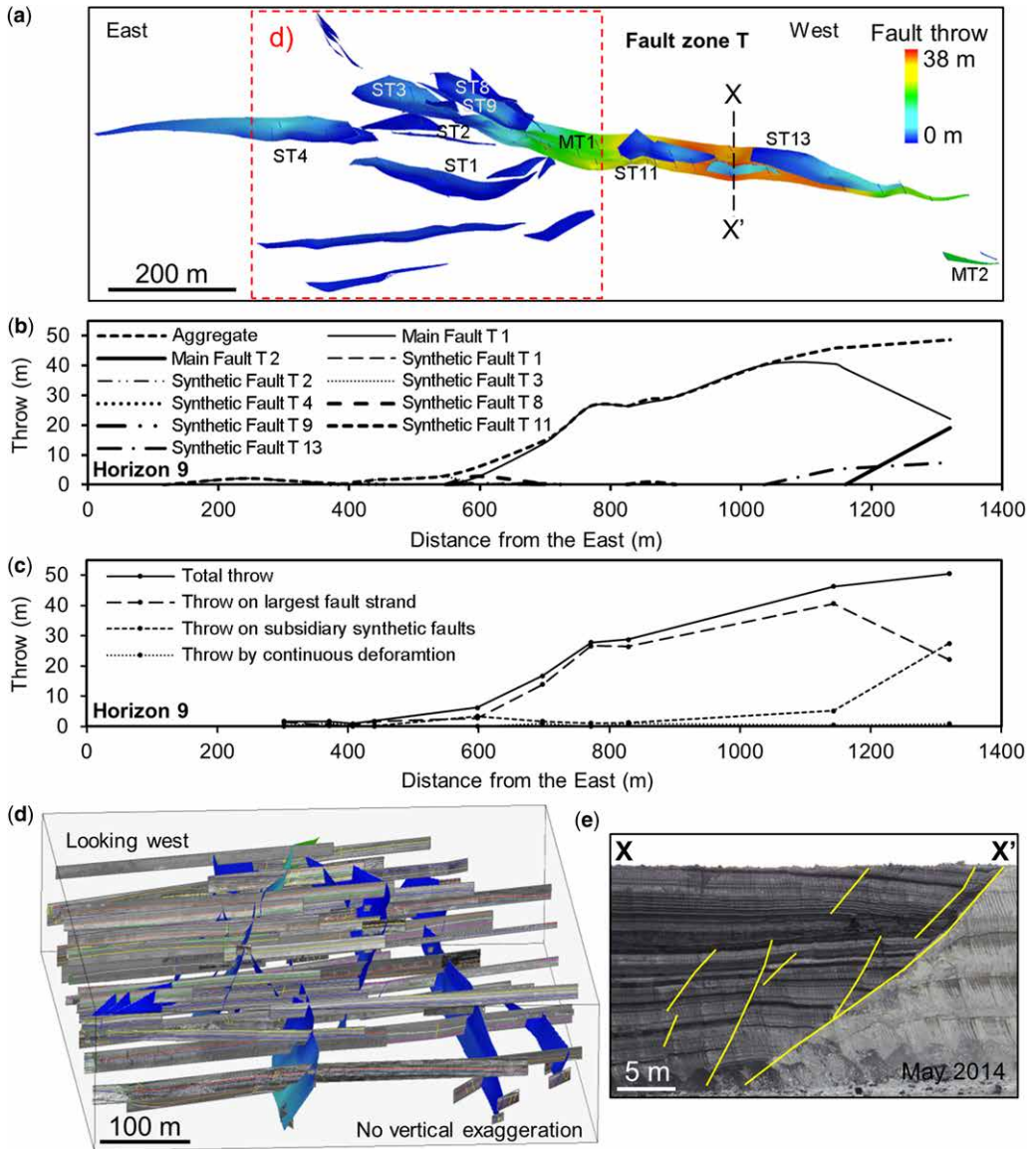


Fig. 10. (a) Plan view of the 3D interpreted fault segments of zone T coloured for throw. (b) Throw profiles of the discontinuous throw along each fault segment and (c) of each throw component along the fault zone measured on Horizon 9. (d) Lateral view of the 'tip area' of fault zone T (location given in (a)) showing the interpreted fault segments and all the imported photographs used for this interpretation. (e) Outcrop photograph across fault zone T at the location labelled in (a).

occupying the lower-left corner of the ternary plot (Fig. 12) accommodate most of the throw by continuous deformation in the form of normal drag (Fig. 6f). Examples of cross-sections through faults that occupy the middle of Figure 12, and consequently have approximately equal contributions from all three components, are shown in Figures

6g, 7e, f and 9e. The ternary plot clearly demonstrates that a high proportion of continuous deformation is generally associated with relatively low total throw, and most of the data associated with a large total throw are located close to the upper corner where most of the throw is accommodated by a dominant fault strand.

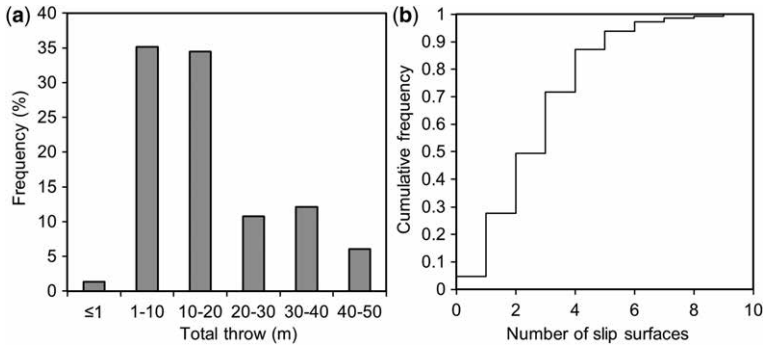


Fig. 11. (a) Histogram of total throw for 148 measurements taken on cross-sections along seven interpreted fault zones in Kardia Mine and (b) cumulative frequency plot of the number of slip surfaces present on each fault zone cross-section.

Throw on largest fault strand

Throw on the largest fault strand increases as the total throw on the fault zone increases (Fig. 13a). The throw on the largest fault encountered on a cross-section through a fault zone with total throw greater than about 20 m varies between 30 and close to 100% of the total throw, but can be very low (even zero) for faults smaller than this (Figs 12 & 13a, b). In general, this percentage increases with increasing total throw. The minimum proportion of the total throw accommodated by the largest fault also increases with increased throw, as indicated by the dashed line in Figure 13b. In Figure

13a, b there is a subset of the data with throws in the 30–40 m range that have anomalously low throws on the largest fault strand and therefore lie below the dashed line in Figure 13b; these data are discussed in more detail below.

The tendency for the largest fault strand to accommodate more of the total throw with increasing zone throw is also apparent when the data are grouped into individual fault zones (Fig. 13c). Cumulative frequency curves of the proportion of throw on the largest fault strand show that smaller displacement fault zones (thin lines in Fig. 13c), with maximum recorded throws from 17 to 23 m, have a wider range of values and, on average,

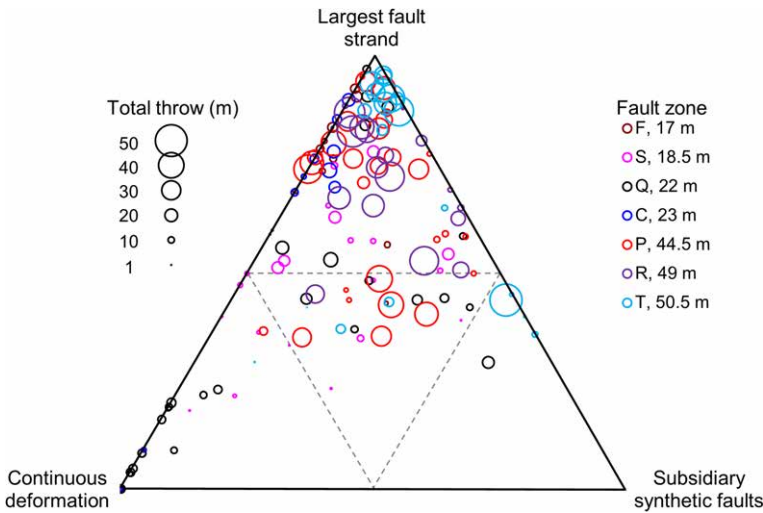


Fig. 12. Ternary diagram showing the relative contribution to the total fault zone throw by the throw on the largest fault strand, the throw on subsidiary synthetic faults and continuous deformation. The bubble size is scaled to total throw and the colours represent different fault zones with maximum throws provided in the legend. The grey dashed lines are the 50% contours.

THROW PARTITIONING ACROSS NORMAL FAULT ZONES

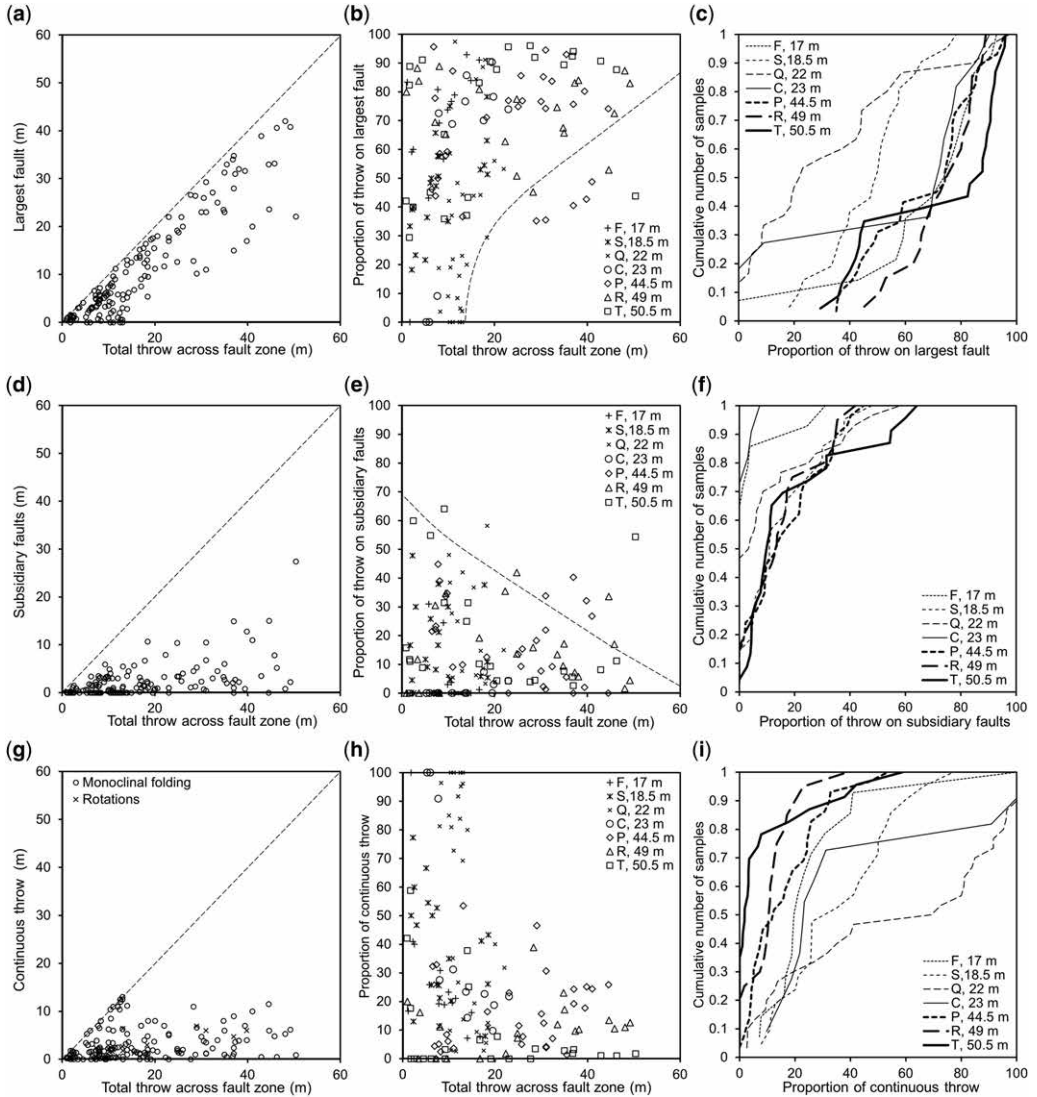


Fig. 13. Graphs illustrating how the the total fault zone throw is partitioned into the throw on the largest fault strand (a–c), subsidiary faults (d–f) and continuous deformation (g–i). Total throw across a fault zone v. throw accommodated by (a) the largest fault strand, (d) subsidiary synthetic faults and (g) continuous deformation recorded on cross-sections through fault zones in Kardia Mine. (b), (e) & (h) are the equivalent data expressed as percentages of the total throw. (c), (f) & (i) are frequency distributions of the proportion of total throw accommodated on (c) the largest fault strand, (f) subsidiary synthetic faults and (i) continuous deformation for each of the seven interpreted fault zones in Kardia Mine. The dashed lines in (b) and (e) are intended to mark the lower (b) and upper (e) limits of the data, highlighting trends in these limits with increasing throw. A collection of data points that lie outside these limits are related to the largest scales of segmentation observed, and are discussed in detail in the text.

lower values than the larger faults (thick lines in Fig. 13c) with throws from 45 to 50 m. These observations indicate that as fault size increases, the contribution of throw on the main fault strand relative to total throw increases, and that the fault zones tend to become progressively more localized.

The cumulative frequency curves in Figure 13c have a range of shapes from smooth curves to curves with pronounced steps. We suggest that this range of shapes reflects the extent of our sampling of the different fault zones. Of the mapped fault zones, only fault zone S has been mapped along its entire

length and the other six fault zones were mapped over a portion of the total fault zone length. Total lengths for the other fault zones are known from borehole-based mapping around the excavated area. Our sampling of fault zones R and P represents more than half of their total length and their maximum throw has been recorded. In contrast, fault zones C, F, Q and T were mapped over about a quarter of their total lengths. As a result, we regard our recorded data for fault zones S, P and R to be more representative than those for the other faults. The curves for these three fault zones demonstrate the concentration of throw onto the largest fault with increasing throw.

Throw on subsidiary synthetic faults

Throw on subsidiary faults observed on individual cross-sections shows a general increase in magnitude with total throw (Fig. 13d): however, its significance relative to the total throw is not clear. Figure 13e suggests, perhaps, that the maximum proportion of throw decreases slightly with increased throw (as indicated by the dashed line). The average contribution of subsidiary faults is, however, relatively constant at about 15%, irrespective of total fault throw (Fig. 14a). Cumulative frequency curves for the proportion of the total throw accommodated by subsidiary faults within individual fault zones are very similar (Fig. 13f), particularly those fault zones that are best sampled (S, P and R; see earlier). These curves indicate that within an individual fault zone, subsidiary faults may account for between 0 and 65% of the total throw irrespective of the size of the fault. This observation suggests that the contribution of subsidiary faults does not change significantly with fault size, at least over the limited scale range represented by the seven sampled fault zones.

Throw by continuous deformation

Continuous deformation, in the form of monoclines, normal drag and bed rotation between fault strands, can account for as much as 12 m throw on the structures observed in the Kardia Mine (Fig. 13g). On cross-sections that record a total throw of less than 12 m, continuous deformation can account for the entire throw. For larger total throws, however, continuous deformation accounts for a progressively smaller proportion of the total throw (Fig. 13h). The relative decrease in the significance of continuous deformation is also apparent when different fault zones are compared (Fig. 13i), and the proportion of total throw accommodated on the smaller faults (S, F and Q) is much more significant than for the fault zones with maximum throws greater than 40 m (T, P and R).

Continuous deformation identified in Figures 6–10 and 12 combines two distinct components: monoclinical folding (or normal drag); and rotation between fault segments (see T_d and T_r , respectively, in Fig. 1b). These two components are noted in Figure 13g. Of the two components, the contribution from monoclinical folding predominates and there are relatively few data for bed rotations. Nevertheless, it appears that the scaling of these two components is different, with the contribution from monoclinical folding attaining its upper limit at 12 m total throw, while the contribution from bed rotation increases with increasing total throw.

Discussion

Fault zone evolution

Taken together (Fig. 14a), our analysis of measurements made on 148 cross-sections through seven fault zones demonstrates that as the displacement on a fault zone increases, the proportion of throw on the largest fault tends to increase, reflecting a progressive localization of strain. The data also demonstrate that the significance of continuous deformation decreases with increasing throw, with a less clear trend for the significance of subsidiary faults. While these aspects of fault evolution are also borne out by comparison between measurements derived from relatively small and large faults (Fig. 13c, f, i), when looked at in detail departures from these overall trends occur, as can be appreciated by inspection of Figure 14b–h. For example, the data for fault zones F, S and T, and to a lesser extent P and C, demonstrate the same trends as the combined dataset, with an increased proportion of ductile deformation and a decreased proportion of throw on the largest fault in areas of low total throw (i.e. close to the tips of the fault zone). These trends, however, are not always apparent for individual faults and, for example, the relative proportions of the different throw components do not appear to be related to the total throw for fault zone R (Fig. 14g). Departures from the general data trend can be attributed to a variety of factors ranging from insufficient sampling, as is likely the case for fault zone Q, to the natural variability in any fault system, which may reflect a host of factors including interaction with adjacent faults and differences in stratigraphic level.

We conclude that our dataset demonstrates progressive localization of strain with increasing fault throw both on the scale of the individual fault zone and for the dataset of all fault zones combined. There are, however, a number of caveats to this model to be considered. Chief among these is the scale range of our sample and, specifically, the

THROW PARTITIONING ACROSS NORMAL FAULT ZONES

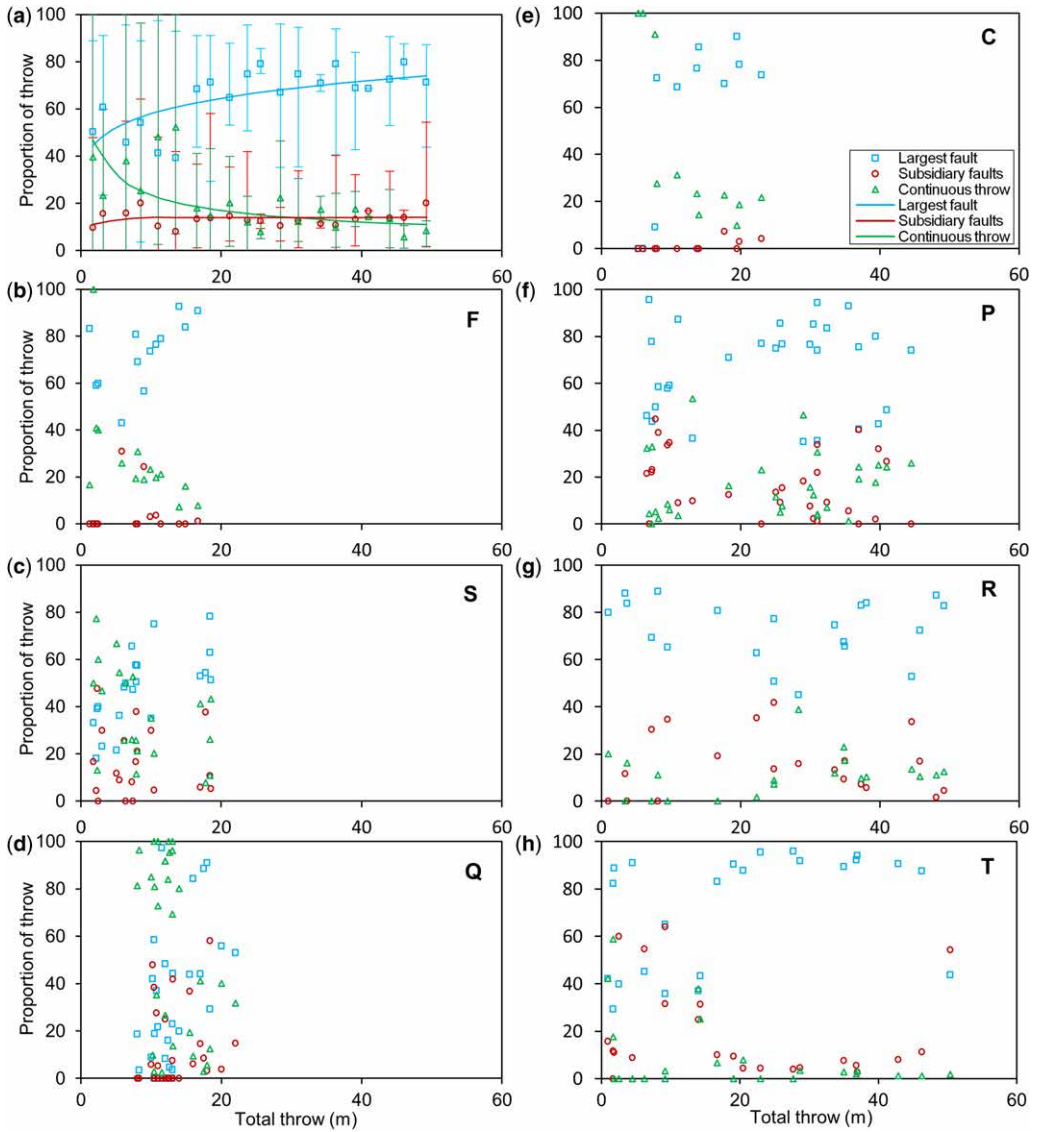


Fig. 14. (a) The contribution of each throw component to the total throw for binned total throw values (2.5 m bins) and corresponding power-law regression curves, showing how the total throw is partitioned into the different throw components for the full range of total throws recorded in the Ptolemais fault zones. The error bars show the minimum and maximum proportions for each binned total throw. (b)–(h) Plots of the total throw across a fault zone v. the throw accommodated by the three different throw components for each fault zone examined.

grouping of fault segments into a fault zone. At outcrop, identification of fault segments as components of a fault zone is often straightforward (e.g. Fig. 6h). However, compilation of outcrop data, map construction and analysis of displacement distributions often indicates interaction between faults that was not apparent in the field, generally because the displacements on the fault strands are small in relation

to the distance between them. For example, segments in fault zone P are clearly kinematically related when seen in map view (Fig. 5), but were not grouped together in the field. Therefore, as described previously, fault segmentation occurs on a wide range of scales (Morley *et al.* 1990; Peacock & Sanderson 1991; Walsh *et al.* 1999; Childs *et al.* 2009), not all of which are apparent at a particular

scale of observation. In the mapping that we have carried out at the Kardia Mine, the largest separation between two fault segments identified as belonging to a single fault zone is 75 m, but there are clear indications of larger-scale segmentation (e.g. see fault zone T above).

The existence of a wide scale range of fault segmentation hinders, to a certain extent, the quantitative analysis of our scale-limited fault zone dataset. In particular, the widest scale of segmentation mapped consists of neutral relay zones or lenses up to about 200 m wide (Fig. 5). In accordance with observations from other faults zones (Childs *et al.* 2009), relays this size on faults with 20–40 m throw are typically intact or only slightly breached, and cross-sections across them therefore represent regions with comparatively poor displacement localization. Since these wide fault zone regions are relatively rare (Fig. 5), there are only a few data through larger (20–40 m throw) faults which are poorly localized (these are the data below the dashed line in Fig. 13b and above the dashed line in Fig. 13e), and these points therefore appear to be outliers of a trend of progressive localization with increasing fault throw. If displacement were to continue to accrue on these faults, then the relays or lenses would become progressively more breached and the displacement across them would become progressively more localized. At these hypothesized larger throws, however, yet more widely spaced zones might be considered part of an individual fault zone (e.g. zones R and T; Fig. 5), and the relay between these would represent a poorly localized region of this hypothetical, much larger throw, fault zone. Hence, the presence of relatively rare, poorly localized regions of individual fault zones even at relatively large throws (Fig. 13b, e) is likely to persist to much larger throws than those mapped in the Kardia Mine, and is evidence of a large-scale range of segmentation within natural fault systems.

Despite the complications associated with a wide-scale range of fault segmentation combined with a limited scale range of observation, our data nevertheless display progressive localization of strain. This localization is clearly expressed by the progressive increase in throw on the largest fault (Fig. 13b) and the decrease in throw accommodated by continuous deformation (Fig. 13h). The role of subsidiary faults is less easy to define and our data indicate that the proportion of throw accommodated by subsidiary faults does not significantly diminish with increasing displacement (Fig. 13e). However, if the outliers (discussed in the previous paragraph), that represent the largest scales of fault segmentation, are removed then a case for a diminished contribution may be strengthened (see the dashed line in Fig. 13e).

Irrespective of whether there is a decrease in the proportion of throw accommodated by subsidiary faults, there is an increase in the absolute values of throw they accommodate (Fig. 13d). There are many potential causes for continued movement on subsidiary faults, including removal of asperities as displacement accrues on a through-going, but irregular, fault surface and fault segmentation over a wide range of scales, as described above. One mechanism that is known to be active in the Kardia Mine is the removal of asperities formed by bedding-parallel slip during normal faulting.

Development of drag

A theme repeatedly addressed in this volume (Childs *et al.* 2016; Ferrill *et al.* 2016; Lăpădat *et al.* 2016; Homberg *et al.* this volume, in press) and in previous publications (Billings 1972) is whether monoclinial, fault-related, folding develops at the tips of propagating faults (Sharp *et al.* 2000; Jackson *et al.* 2006; White & Crider 2006; Ferrill *et al.* 2012) or in response to frictional drag after a through-going fault has been established. It should be possible to differentiate between these models on the basis of the distribution of continuous deformation over the fault surface. If the frictional model would apply, then continuous deformation is expected to increase with increasing total displacement towards the centre of a fault surface. Continuous displacement within the studied fault zones shows a variety of distributions. In fault zone R (Figs 9c & 14g), continuous deformation decreases towards the tip of the fault zone from a maximum close to the centre of the fault. In contrast, continuous deformation is at a maximum at the mapped tip of fault zone C (Figs 8 & 14e). We also find that ductile deformation and monoclinial folding can occur between fault strands, as illustrated by fault zone Q (Fig. 6d, e). In this case, which is discussed in more detail in Childs *et al.* (2016), monoclinial folding may be between two segments of a fault zone that propagated upwards.

While individual fault zones display a range of distributions that individually support different models for the development of drag, our data, when taken together (Fig. 13h), clearly indicate that the proportion of total throw accommodated by folding decreases with increasing throw. Our observations do not, however, suggest that fault tips are always associated with folding, and there are many examples of structures with small total throws where folding is absent and also examples where monoclinial folding is dominant (e.g. Fig. 8b). Our data therefore suggest that, in general, monoclinial folding is associated with the earlier stages of fault zone development and, while it is reduced in significance as displacement increases, it can continue to amplify.

THROW PARTITIONING ACROSS NORMAL FAULT ZONES

We speculate that an increase in drag with increased displacement is not frictional in the sense of the frictional properties of the fault rock/surface, but is related to fault geometry, developing at particular locations within an array of fault segments (e.g. within relay zones).

Summary and conclusions

Characterization of fault zone structure requires 3D mapping of the displacement distribution and partitioning along, within and around individual segments or splays that comprise a zone. Our analysis of fault zones in the Kardia Mine, Ptolemais Basin, provides unprecedented outcrop-scale access to the 3D geometry of oilfield-scale faults and, in combination with quantification of throw partitioning along these fault zones, improves our understanding of fault zone evolution.

The main conclusions obtained from the quantitative analysis of throw partitioning along seven fault zones are:

- Throw partitioning decreases with increased throw, consistent with progressive strain localization during fault growth within the scale range observable in this mine.
- The degree of throw partitioning and the rapid lateral variations in throw partitioning over a fault zone are related primarily to the range of scales of segmentation of the initial fault.
- The contribution of continuous deformation to total throw decreases as the total throw increases, suggesting that continuous deformation, such as normal drag, develops during the early stages of fault zone development.
- The throw on subsidiary synthetic faults increases with increasing total throw and its contribution to total throw appears to be more or less constant within the scale range observed in this study.

This work was carried out as part of the Earth and Natural Sciences Doctoral Studies Programme, funded by the Higher Education Authority (HEA) through the Programme for Research at Third Level Institutions, Cycle 5 (PRTL1-5), co-funded by the European Regional Development Fund (ERDF). The work was also funded by the multi-company QUAFF project, sponsored by Anadarko, BG, BP, ConocoPhillips, ENI, ExxonMobil, Marathon, Statoil, Total and Woodside. C. Childs is funded by Tullow Oil. The authors would like to thank Badley Geoscience Ltd for the use of the TrapTester6 software. The authors also thank the Public Power Corporation (ΔΕΗ/ΑΚΠΑ) for permission to work in the mines, and the corporation's employees for their hospitality and assistance in the field over the last 4 years. We thank other members of the Fault Analysis Group for field assistance and useful discussions, Mette Bundgaard Kristensen for drawing our attention to the mines, and Joris Steenbrink for introducing us to

the Ptolemais Basin. We also thank Jonathan Imber and an anonymous reviewer for their helpful reviews.

References

- ALSOP, G.I. & MARCO, S. 2013. Seismogenic slump folds formed by gravity-driven tectonics down a negligible subaqueous slope. *Tectonophysics*, **605**, 48–69, <http://doi.org/10.1016/j.tecto.2013.04.004>
- ANASTOPOULOS, J. & KOUKOUZAS, N. 1972. *Economic Geology of the Southern Part Ptolemais Lignite Basin (Macedonia – Greece)*. Geological & Geophysical Research, IGME, Athens.
- BAILEY, W., WALSH, J. & MANZOCCHI, T. 2005. Fault populations, strain distribution and basement fault reactivation in the East Pennines Coalfield, UK. *Journal of Structural Geology*, **27**, 913–928, <http://doi.org/10.1016/j.jsg.2004.10.014>
- BARNETT, J.A.M., MORTIMER, J., RIPPON, J.H., WALSH, J.J. & WATTERSON, J. 1987. Displacement geometry in the volume containing a single normal fault. *American Association of Petroleum Geologists Bulletin*, **71**, 925–937.
- BEN-ZION, Y. & SAMMIS, C.G. 2003. Characterization of fault zones. *Pure and Applied Geophysics*, **160**, 677–715, <http://doi.org/10.1007/PL00012554>
- BILLINGS, M.P. 1972. *Structural Geology*. 3rd edn. Prentice-Hall, Englewood Cliffs, NJ.
- BRANDES, C. & TANNER, D.C. 2014. Fault-related folding: a review of kinematic models and their application. *Earth-Science Reviews*, **138**, 352–370, <http://doi.org/10.1016/j.earscirev.2014.06.008>
- CAINE, J.S., EVANS, J.P. & FORSTER, C.B. 1996. Fault zone architecture and permeability structure. *Geology*, **24**, 1025–1028, [http://doi.org/10.1130/0091-7613\(1996\)024<1025:FZAAPS>2.3.CO;2](http://doi.org/10.1130/0091-7613(1996)024<1025:FZAAPS>2.3.CO;2)
- CARTWRIGHT, J.A., MANSFIELD, C. & TRUDGILL, B. 1996. The growth of normal faults by segment linkage. In: BUCHANAN, P.G. & NIEUWLAND, D.A. (eds) *Modern Developments in Structural Interpretation, Validation and Modelling*. Geological Society, London, Special Publications, **99**, 163–177, <http://doi.org/10.1144/GSL.SP.1996.099.01.13>
- CHILDS, C., WATTERSON, J. & WALSH, J.J. 1995. Fault overlap zones within developing normal fault systems. *Journal of the Geological Society, London*, **152**, 535–549, <http://doi.org/10.1144/gsjgs.152.3.0535>
- CHILDS, C., WALSH, J.J. & WATTERSON, J. 1997. Complexity in fault zone structure and implications for fault seal prediction. In: MØLLER-PEDERSEN, P. & KOESTLER, A.G. (eds) *Hydrocarbon Seals Importance for Exploration and Production*. Norwegian Petroleum Society Special Publications, **7**, 61–72, [http://doi.org/10.1016/S0928-8937\(97\)80007-0](http://doi.org/10.1016/S0928-8937(97)80007-0)
- CHILDS, C., MANZOCCHI, T., WALSH, J.J., BONSON, C.G., NICOL, A. & SCHÖPFER, M.P.J. 2009. A geometric model of fault zone and fault rock thickness variations. *Journal of Structural Geology*, **31**, 117–127, <http://doi.org/10.1016/j.jsg.2008.08.009>
- CHILDS, C., MANZOCCHI, T., NICOL, A., WALSH, J.J., SODEN, A.M., CONNEALLY, J.C. & DELOGKOS, E. 2016. The relationship between normal drag, relay ramp aspect ratio and fault zone structure. In: CHILDS,

- C., HOLDSWORTH, R.E., JACKSON, C.A.-L., MANZOCCHI, T., WALSH, J.J. & YIELDING, G. (eds) *The Geometry and Growth of Normal Faults*. Geological Society, London, Special Publications, **439**. First published online August 17, 2016, <http://doi.org/10.1144/SP439.16>
- DIAMANTOPOULOS, A., KROHE, A. & DIMITRAKOPOULOS, D. 2013. Deformation partitioning in a transtension-dominated tectonic environment: the illustrative kinematic patterns of the Neogene–Quaternary Ptolemais Basin (northern Greece). *Journal of the Geological Society, London*, <http://doi.org/10.1144/jgs2012-138>
- DOUTSOS, T. & KOUKOUVELAS, I. 1998. Fractal analysis of normal faults in northwestern Aegean area, Greece. *Journal of Geodynamics*, **26**, 197–216, [http://doi.org/10.1016/S0264-3707\(97\)00052-5](http://doi.org/10.1016/S0264-3707(97)00052-5)
- EVANS, J.P. 1990. Thickness–displacement relationships for fault zones. *Journal of Structural Geology*, **12**, 1061–1065, [http://doi.org/10.1016/0191-8141\(90\)90101-4](http://doi.org/10.1016/0191-8141(90)90101-4)
- FERRILL, D.A., SMART, K.J. & NECSOIU, M. 2008. Displacement–length scaling for single-event fault ruptures: insights from Newberry Springs Fault Zone and implications for fault zone structure. In: WIBBERLEY, C.A.J., KURZ, W., IMBER, J., HOLDSWORTH, R.E. & COLLETTINI, C. (eds) *The Internal Structure of Fault Zones: Implications for Mechanical and Fluid-Flow Properties*. Geological Society, London, Special Publications, **299**, 113–122, <http://doi.org/10.1144/SP299.7>
- FERRILL, D.A., MORRIS, A.P., MCGINNIS, R.N., SMART, K.J. & WARD, W.C. 2011. Fault zone deformation and displacement partitioning in mechanically layered carbonates: the Hidden Valley fault, central Texas. *American Association of Petroleum Geologists Bulletin*, **95**, 1383–1397, <http://doi.org/10.1306/12031010065>
- FERRILL, D.A., MORRIS, A.P. & MCGINNIS, R.N. 2012. Extensional fault-propagation folding in mechanically layered rocks: the case against the frictional drag mechanism. *Tectonophysics*, **576–577**, 78–85, <http://doi.org/10.1016/j.tecto.2012.05.023>
- FERRILL, D.A., MORRIS, A.P., MCGINNIS, R.N. & SMART, K.J. 2016. Myths about normal faulting. In: CHILDS, C., HOLDSWORTH, R.E., JACKSON, C.A.-L., MANZOCCHI, T., WALSH, J.J. & YIELDING, G. (eds) *The Geometry and Growth of Normal Faults*. Geological Society, London, Special Publications, **439**. First published online March 30, 2016, <http://doi.org/10.1144/SP439.12>
- FREEMAN, S.R., HARRIS, S.D. & KNIPE, R.J. 2008. Fault seal mapping: incorporating geometric and property uncertainty. In: ROBINSON, A., GRIFFITHS, P., PRICE, S., HEGRE, J. & MUGGERIDGE, A. (eds) *The Future of Geological Modelling in Hydrocarbon Development*. Geological Society, London, Special Publications, **309**, 5–38, <http://doi.org/10.1144/SP309.2>
- HAMBLIN, W.K. 1965. Origin of ‘reverse drag’ on the downthrown side of normal faults. *Geological Society of America Bulletin*, **76**, 1145–1164, [http://doi.org/10.1130/0016-7606\(1965\)76\[1145:OORDOT\]2.0.CO;2](http://doi.org/10.1130/0016-7606(1965)76[1145:OORDOT]2.0.CO;2)
- HOMBERG, C., SCHNYDER, J., ROCHE, V. & LÉONARDI, V. In press. The brittle and ductile components of displacement along fault zones. In: CHILDS, C., HOLDSWORTH, R.E., JACKSON, C.A.-L., MANZOCCHI, T., WALSH, J.J. & YIELDING, G. (eds) *The Geometry and Growth of Normal Faults*. Geological Society, London, Special Publications, **439**, <http://doi.org/10.1144/SP439.21>
- JACKSON, C.A.L., GAWTHORPE, R.L. & SHARP, I.R. 2006. Style and sequence of deformation during extensional fault-propagation folding: examples from the Hammam Faraun and El-Qaa fault blocks, Suez Rift, Egypt. *Journal of Structural Geology*, **28**, 519–535, <http://doi.org/10.1016/j.jsg.2005.11.009>
- JAMISON, W.R. & STEARNS, D.W. 1982. Tectonic deformation of Wingate Sandstone, Colorado National Monument. *American Association of Petroleum Geologists Bulletin*, **66**, 2584–2608.
- KIM, Y. & SANDERSON, D. 2005. The relationship between displacement and length of faults: a review. *Earth-Science Reviews*, **68**, 317–334, <http://doi.org/10.1016/j.earscirev.2004.06.003>
- KRISTENSEN, M.B. 2005. *Soft Sediment Faulting: Investigation of the 3D Geometry and Fault Zone Properties*. PhD thesis, Department of Earth Sciences, University of Aarhus, Denmark.
- LÄPÄDAT, A., IMBER, J., YIELDING, G., IACOPINI, D., MCCAFFREY, K.J.W., LONG, J.J. & JONES, R.R. 2016. Occurrence and development of folding related to normal faulting within a mechanically heterogeneous sedimentary sequence: a case study from Inner Moray Firth, UK. In: CHILDS, C., HOLDSWORTH, R.E., JACKSON, C.A.-L., MANZOCCHI, T., WALSH, J.J. & YIELDING, G. (eds) *The Geometry and Growth of Normal Faults*. Geological Society, London, Special Publications, **439**. First published online September 26, 2016, <http://doi.org/10.1144/SP439.18>
- MANZOCCHI, T., HEATH, A.E., PALANANTHAKUMAR, B., CHILDS, C. & WALSH, J.J. 2008. Faults in conventional flow simulation models: a consideration of representational assumptions and geological uncertainties. *Petroleum Geoscience*, **14**, 91–110, <http://doi.org/10.1144/1354-079306-775>
- MANZOCCHI, T., CHILDS, C. & WALSH, J.J. 2010. Faults and fault properties in hydrocarbon flow models. In: YARDLEY, B., MANNING, C. & GARVEN, G. (eds) *Frontiers in Geofluids*. Wiley-Blackwell, Oxford, UK, 94–113, <http://doi.org/10.1002/9781444394900.ch8>
- MARCHAL, D., GUIRAUD, M. & RIVES, T. 2003. Geometric and morphologic evolution of normal fault planes and traces from 2D to 4D data. *Journal of Structural Geology*, **25**, 135–158, [http://doi.org/10.1016/S0191-8141\(02\)00011-1](http://doi.org/10.1016/S0191-8141(02)00011-1)
- MCGRATH, A.G. & DAVIDSON, I. 1995. Damage zone geometry around fault tips. *Journal of Structural Geology*, **17**, 1011–1024, [http://doi.org/10.1016/0191-8141\(94\)00116-H](http://doi.org/10.1016/0191-8141(94)00116-H)
- MERCIER, J.L., SOREL, D., VERGELY, P. & SIMEAKIS, K. 1989. Extensional tectonic regimes in the Aegean basins during the Cenozoic. *Basin Research*, **2**, 49–71, <http://doi.org/10.1111/j.1365-2117.1989.tb00026.x>
- MORLEY, C.K., NELSON, R.A., PATTON, T.L. & MUNN, S.G. 1990. Transfer zones in the East African rift system and their relevance to hydrocarbon exploration in rifts. *AAPG Bulletin*, **74**, 1234–1253, <http://doi.org/10.1306/0C9B2475-1710-11D7-8645000102C1865D>

THROW PARTITIONING ACROSS NORMAL FAULT ZONES

- MOUNTRAKIS, D., PAVLIDES, S., ZOUROS, N., ASTARAS, T. & CHATZIPETROS, A. 1998. Seismic fault geometry and kinematics of the 13 May 1995 western Macedonia (Greece) earthquake. *Journal of Geodynamics*, **26**, 175–196, [http://doi.org/10.1016/S0264-3707\(97\)00082-3](http://doi.org/10.1016/S0264-3707(97)00082-3)
- PAVLIDES, S.B. 1985. *Neotectonic Evolution of the Florina–Vegoritís–Ptolemais Basins*. PhD thesis, University of Thessaloniki, Greece.
- PAVLIDES, S.B. & MOUNTRAKIS, D.M. 1987. Extensional tectonics of northwestern Macedonia, Greece, since the late Miocene. *Journal of Structural Geology*, **9**, 385–392, [http://doi.org/10.1016/0191-8141\(87\)90115-5](http://doi.org/10.1016/0191-8141(87)90115-5)
- PAVLIDES, S.B., ZOUROS, N.C., CHATZIPETROS, A.A., KOSTOPOULOS, D.S. & MOUNTRAKIS, D.M. 1995. The 13 May 1995 western Macedonia, Greece (Kozani Grevena) earthquake; preliminary results. *Terra Nova*, **7**, 544–549, <http://doi.org/10.1111/j.1365-3121.1995.tb00556.x>
- PEACOCK, D.C.P. & SANDERSON, D.J. 1991. Displacements, segment linkage and relay ramps in normal fault zones. *Journal of Structural Geology*, **13**, 721–733, [http://doi.org/10.1016/0191-8141\(91\)90033-F](http://doi.org/10.1016/0191-8141(91)90033-F)
- PEACOCK, D.C.P., KNIPE, R.J. & SANDERSON, D.J. 2000. Glossary of normal faults. *Journal of Structural Geology*, **22**, 291–305, [http://doi.org/10.1016/S0191-8141\(00\)80102-9](http://doi.org/10.1016/S0191-8141(00)80102-9)
- RECHES, Z. & EIDELMAN, A. 1995. Drag along faults. *Tectonophysics*, **247**, 145–156.
- SCHULTZ, R.A., SOLIVA, R., FOSSEN, H., OKUBO, C.H. & REEVES, D.M. 2008. Dependence of displacement–length scaling relations for fractures and deformation bands on the volumetric changes across them. *Journal of Structural Geology*, **30**, 1405–1411, <http://doi.org/10.1016/j.jsg.2008.08.001>
- SEEBECK, H., NICOL, A., WALSH, J.J., CHILDS, C., BEE-THAM, R.D. & PETTINGA, J. 2014. Fluid flow in fault zones from an active rift. *Journal of Structural Geology*, **62**, 52–64, <http://doi.org/10.1016/j.jsg.2014.01.008>
- SHARP, I.R., GAWTHORPE, R.L., UNDERHILL, J.R. & GUPTA, S. 2000. Fault-propagation folding in extensional settings: examples of structural style and synrift sedimentary response from the Suez rift, Sinai, Egypt. *Geological Society of America Bulletin*, **112**, 1877–1899, [http://doi.org/10.1130/0016-7606\(2000\)112<1877:FPFIES>2.0.CO;2](http://doi.org/10.1130/0016-7606(2000)112<1877:FPFIES>2.0.CO;2)
- SHIPTON, Z.K. & COWIE, P.A. 2001. Damage zone and slip-surface evolution over mm to km scales in high-porosity Navajo sandstone, Utah. *Journal of Structural Geology*, **23**, 1825–1844, [http://doi.org/10.1016/S0191-8141\(01\)00035-9](http://doi.org/10.1016/S0191-8141(01)00035-9)
- STEENBRINK, J., VAN VUGT, N., HILGEN, F.J., WIJBRANS, J.R. & MEULENKAMP, J.E. 1999. Sedimentary cycles and volcanic ash beds in the Lower Pliocene lacustrine succession of Ptolemais (NW Greece): discrepancy between $^{40}\text{Ar}/^{39}\text{Ar}$ and astronomical ages. *Palaeogeography, Palaeoclimatology, Palaeoecology*, **152**, 283–303, [http://doi.org/10.1016/S0031-0182\(99\)00044-9](http://doi.org/10.1016/S0031-0182(99)00044-9)
- VAN VUGT, N., STEENBRINK, J., LANGEREIS, C.G., HILGEN, F.J. & MEULENKAMP, J.E. 1998. Magnetostratigraphy-based astronomical tuning of the early Pliocene lacustrine sediments of Ptolemais (NW Greece) and bed-to-bed correlation with the marine record. *Earth and Planetary Science Letters*, **164**, 535–551, [http://doi.org/10.1016/S0012-821X\(98\)00236-2](http://doi.org/10.1016/S0012-821X(98)00236-2)
- WALSH, J.J. & WATTERSON, J. 1991. Geometric and kinematic coherence and scale effects in normal fault systems. In: ROBERTS, A.M., YIELDING, G. & FREEMAN, B. (eds) *The Geometry of Normal Faults*. Geological Society, London, Special Publications, **56**, 193–203, <http://doi.org/10.1144/GSL.SP.1991.056.01.13>
- WALSH, J.J., WATTERSON, J., BAILEY, W.R. & CHILDS, C. 1999. Fault relays, bends and branch-lines. *Journal of Structural Geology*, **21**, 1019–1026, [http://doi.org/10.1016/S0191-8141\(99\)00026-7](http://doi.org/10.1016/S0191-8141(99)00026-7)
- WALSH, J.J., NICOL, A. & CHILDS, C. 2002. An alternative model for the growth of faults. *Journal of Structural Geology*, **24**, 1669–1675, [http://doi.org/10.1016/S0191-8141\(01\)00165-1](http://doi.org/10.1016/S0191-8141(01)00165-1)
- WALSH, J.J., BAILEY, W., CHILDS, C., NICOL, A. & BONSON, C. 2003. Formation of segmented normal faults: a 3-D perspective. *Journal of Structural Geology*, **25**, 1251–1262, [http://doi.org/10.1016/S0191-8141\(02\)00161-X](http://doi.org/10.1016/S0191-8141(02)00161-X)
- WHITE, I.R. & CRIDER, J.G. 2006. Extensional fault-propagation folds: mechanical models and observations from the Modoc Plateau, northeastern California. *Journal of Structural Geology*, **28**, 1352–1370, <http://doi.org/10.1016/j.jsg.2006.03.028>
- WIBBERLEY, C.A.J., YIELDING, G. & DI TORO, G. 2008. Recent advances in the understanding of fault zone internal structure: a review. In: WIBBERLEY, C.A.J., KURZ, W., IMBER, J., HOLDSWORTH, R.E. & COLLETTINI, C. (eds) *The Internal Structure of Fault Zones: Implications for Mechanical and Fluid-Flow Properties*. Geological Society, London, Special Publications, **299**, 5–33, <http://doi.org/10.1144/SP299.2>